Relationship Between Cone Loss and Microvasculature Change in Retinitis Pigmentosa

Rui Lin, Meixiao Shen, Deng Pan, Su-Zhong Xu, Ren-Juan Shen, Yilei Shao, Ce Shi, Fan Lu, and Zi-Bing Jin

The Eye Hospital, School of Ophthalmology and Optometry, Wenzhou Medical University, National Center for International Research in Regenerative Medicine and Neurogenetics, National Clinical Research Center for Ophthalmology, State Key Laboratory of Ophthalmology, Optometry and Visual Science, Wenzhou, China

Correspondence: Zi-Bing Jin, The Eye Hospital, School of Ophthalmology and Optometry, Wenzhou Medical University, Number 270, West Xueyuan Road, Wenzhou, Zhejiang, 325027;
jinzb@mail.eye.ac.cn.
Fan Lu, The Eye Hospital, School of Ophthalmology and Optometry, Wenzhou Medical University, Number 270, West Xueyuan Road, Wenzhou, Zhejiang, 325027;
lufan@mail.eye.ac.cn.

Submitted: March 18, 2019
Accepted: September 3, 2019

Citation: Lin R, Shen M, Pan D, et al. Relationship between cone loss and microvasculature change in retinitis pigmentosa. *Invest Ophthalmol Vis Sci*. 2019;60:4520–4531. https://doi.org/10.1167/iovs.19-27114

Purpose. To objectively quantify cone density (CD) and microvascular density (MVD) in normal subjects and patients with moderate or severe retinitis pigmentosa (RP) by adaptive optics (AO) and optical coherence tomography angiography (OCTA) and to evaluate the changes in the parafoveal regions.

Method. Thirty-seven eyes from 20 RP patients and 54 eyes from 29 age-matched healthy participants underwent AO fundus and OCTA imaging. AO images covering a 3-mm-diameter area centered on the fovea were subdivided into 5 equidistant concentric rings (C1–C5). An automated algorithm was used to quantify the mean cone density (mCD; cells/mm^2). Macular MVDs (%) in the superficial capillary plexus (SCP) and deep capillary plexus (DCP) were assessed by OCTA.

Results. In the moderate RP group, CDs in C2 and C3 were each significantly lower than in the normal group (both $P < 0.05$). In the severe RP group, CDs were significantly lower than in normal eyes in each concentric ring (all $P < 0.001$; C1–C5). In both RP groups, MVDs were significantly lower than in normal eyes for both the SCP and DCP (both $P < 0.05$). The mean CD was significantly correlated with the MVD in the DCP ($r = 0.43$; $P = 0.028$) but not in the SCP ($r = -0.19$, $P = 0.323$).

Conclusions. Decreased CD was present in the moderate and severe RP groups. This was accompanied by a decreased MVD in the DCP. Direct assessment of photoreceptors in RP patients by high-resolution imaging technologies is crucial for the future development of RP therapeutics.

Keywords: adaptive optics, optical coherence tomography angiography, retinitis pigmentosa, visual acuity, pathophysiology

Retinitis pigmentosa (RP) is a genetically heterogeneous group of retinal degenerative disorders that lead to incurable blindness.[1] Clinically, RP manifests with night blindness in adolescence, tunnel vision, and a gradual reduction of central vision. These alterations reflect the progressive degeneration of photoreceptors and retinal pigment epithelium (RPE) cells, attenuation of the retinal vessels, sclerosis, and atrophy of the choriocapillaris.[2] However, the underlying developmental processes and progression remain unknown. Once the photoreceptor degeneration is triggered, no existing treatment can reverse it.

As a part of the central nervous system, the retina remodels in response to the pathologic events in RP.[3,4] Stone et al.[5] found that vascular remodeling and subsequent vessel attenuation may be the result of a loss of synaptic input secondary to photoreceptor cell death. Milam et al.[2] and Grunwald et al.[6] hypothesized that anatomic and functional changes in the retinal vessels of RP patients were secondary to the process of photoreceptor degeneration. However, Cellini et al.[7] found that ocular blood flow was reduced more than would be expected due to retinal atrophy.

Clearly, the relationship between cone photoreceptor and retinal microcirculation is not well known. However, high-resolution imaging technology enables a better understanding of the relationship between retinal structure and microvascular network, and it has been used for the diagnosis and monitoring of RP in clinics. Aizawa et al.[8] and De Rojas et al.[9] used spectral-domain optical coherence tomography (SD-OCT) to show that the deterioration of vision in patients with RP was related to the loss of the inner segment ellipsoid zone (EZ). Hood et al.[10] reported that OCT images showed that late-stage RP was characterized by the complete loss of both the outer segments and the outer nuclear layer. These results indicated the presence of retinal remodeling in RP. However, detailed mapping of the remaining cones in RP patients is still lacking.[11] A major reason for this is that irregularities of the optics in human eyes limit the resolution of retinal images acquired by SD-OCT.[12] Adaptive optics (AO) compensates for optical aberrations and enables the observation of cellular structures in living human eyes.[13] The integration of AO with flood-illumination fundus photography and scanning laser ophthalmoscopy (AOSLO) provides enhanced en face retinal imaging. In addition, with the development of OCT angiography (OCTA), high-resolution, depth-resolved images of the retinal vascular layers can be acquired quickly and noninvasively.[14,15] Previous cross-sectional OCTA studies showed that the superficial and

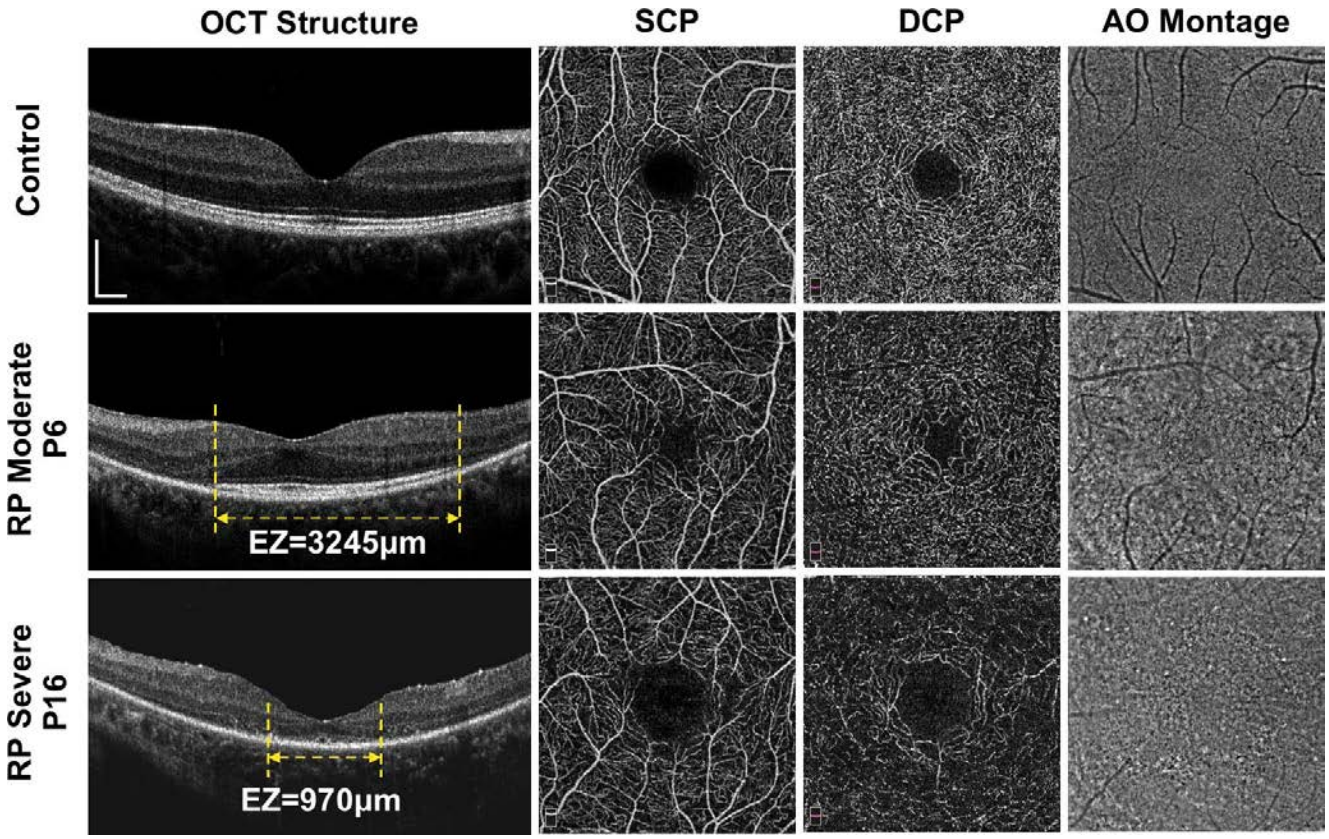

FIGURE 1. Representative OCT structural images, OCTA images, and AO montage images in healthy (*top row*), moderate (*middle row*), and severe (*bottom row*) RP eyes. SCP, superficial capillary plexus; DCP, deep capillary plexus; AO, adaptive optics; EZ, ellipsoid zone.

deep capillary plexus densities (SCP and DCP, respectively) are decreased in both early- and late-stage RP.[16–18] However, these studies did not evaluated the association of these changes with photoreceptor density in the posterior pole of the fundus.

To better understand the pathogenesis of RP, we investigated the organization and distribution of the photoreceptors and the microvascular network by using multiple retinal imaging methods, including commercial flood-illuminated AO and OCTA. This study was designed to quantify the cone density (CD) and microvascular density (MVD) in corresponding parafoveal areas of normal and RP eyes.

METHODS

This cross-sectional study was approved by the Medical Ethics Committee of the Eye Hospital, Wenzhou Medical University, and written informed consent was obtained from all recruited subjects after a thorough explanation of the procedure. All research procedures adhered to the tenets of the Declaration of Helsinki.

Participants

Twenty-one patients with RP and 29 age-matched healthy volunteers were enrolled in the study. The diagnosis of RP was based on clinical symptoms, family history, typical fundus features, full-field electroretinography recordings (according to the standards outlined by the International Society for Clinical Electrophysiology of Vision[19]), SD-OCT, and molecular genetic testing by targeted exome sequencing as previously described.[20,21]

Genomic DNA was extracted from peripheral blood using a whole-blood DNA Extraction kit (Simgen, Hangzhou, China). As described previously,[20] targeted exome sequencing was then performed followed by bioinformatics analysis, Sanger sequencing validation, and cosegregation analysis.

All participants underwent ophthalmologic examination, including best-corrected visual acuity (BCVA), slit-lamp biomicroscopy, color fundus photography, axial length (AL) measurement using the IOL Master (Carl Zeiss Meditec, Jena, Germany), OCTA (RTVue-XR Avanti; Optovue, Inc., Fremont, CA, USA), and AO imaging system (rtx1; Imagine Eyes, Orsay, France).

An experienced ophthalmologist (S.Z.X.) divided the patients into two severity groups based on the EZ width. The "moderate group" was defined as having an EZ width greater than 1500 μm, and the "severe group" was defined as having an EZ width lower than 1500 μm (Fig. 1).

Exclusion criteria included the absence of necessary data, substantial media opacities, corneal scars, severe vitreous floaters (visible floater shadows), and pseudophakia. Patients with cone dystrophy, cone-rod dystrophy, choroideremia, Stargardt disease, and Best disease were excluded. Patients with systemic disease leading to retinal degeneration and the use of medications, such as chloroquine or hydroxychloroquine, that affect macular function were also excluded.

AO Image Acquisition and Cone Structure Analysis

The macular cone mosaic was imaged with a flood-illuminated rtx1 AO retinal camera. Using software provided by the system manufacturer (CK v0.1 and AO detect v0.1; Imagine Eyes), we constructed the final image as the average of 40 separate

images of the same area. Raw images with eye blinking and saccades artifacts were excluded before averaging. A 10° field of the central macula was imaged with a series of 9 images of 4° × 4° (1200 × 1200 μm) with an overlap of 75% between adjacent images. The final image of the 10° field was montaged from these 9 images by using the montage tool in i2k Retina Pro (DualAlign LLC, Clifton Park, NY, USA).

Image Analysis

On each montaged image, cone labeling was performed using an algorithm implemented with the image processing toolbox in Matlab (MathWorks, Natick, MA, USA), similar to a previously described method.[22,23] First, the raw averaged image was preprocessed using adaptive[24] and multiple-scale[25] digital filters to reduce the background noise and smooth the image. The second step of the algorithm was to search for local maxima on the preprocessed image.[26] A maximum was defined as a pixel with an intensity that was no less than its neighbors. In this step, the algorithm first searched all pixels in the image in a search window of 3 × 3 pixels, comparing each one with the adjacent pixels and labeling eligible pixels. A filter window of 7 × 7 pixels was applied to remove the invalid points. If more than one maximum was found in the filter window, the algorithm would label the pixel that had the highest intensity as the valid one. Finally, the algorithm removed the invalid maxima. In this step, a threshold based on the grayscale-value variance of each maximum's vicinity was used to filter the invalid maxima.[27] The pixel coordinates were then recorded, and the CD was estimated. The spatial distribution of these point coordinates was then analyzed as the CD (cells/mm^2) calculated on Voronoi diagrams (Supplementary Fig. S1). To avoid overestimating the hyperreflective spots in the AO images, we visually checked the cones labeled by the automated algorithm. If any hyperreflective spots were marked, we removed them manually. We did not mark additional cones that might have been missed the automated algorithm.

Regional Analysis

To obtain accurate scan lengths, we corrected the magnification effect in each eye using the adjusted AL method reported by Bennett et al.[28] To better estimate CD, the retina was divided into several regions. We did not assess the CD within 400 μm of the foveal center due to the limit of resolution of the rtx1 systems.[29–32] The regional sampling method was previously described.[33] The area within an annulus of 0.4- to 2.4-mm diameter was defined as the total annular zone (TAZ) in a 3 × 3-mm area (Fig. 2A). The TAZ was further divided into five concentric rings and four quadrants to estimate the regional CD distribution in more detail. The width of each concentric ring (corresponding to C1, C2, C3, C4, and C5 in Fig. 2B) was 0.2 mm. The four parafoveal sectors corresponded to the 90° arcuate quadrants identified as superior (S), temporal (T), inferior (I), and nasal (N) (Fig. 2C). Cone counts in the TAZ were converted into local densities by calculating the number per square millimeter (cones/mm^2). The image of the left eye was flipped horizontally to match the quadrants of the right eye for the purpose of definition and averaging. The mean CD (mCD) was calculated in the TAZ, the five concentric rings, and the four quadrants.

OCTA Image Acquisition and Processing

After AO camera examination, the same operator performed OCTA imaging using the AngioVue. The AngioVue utilizes a motion contrast technique based on the OCTA algorithm known as split-spectrum amplitude-decorrelation angiography[34] and provides noninvasive retinal vasculature and microvasculature characterization. A high-resolution three-dimensional visualization of the retinal vascular perfusion at the capillary level was generated by the AngioVue software (version 2017.1.0.155). This version also used projection-resolved OCTA to significantly suppress projection artifacts, thus allowing for proper segmentation of retinal structures.[35] Retinal OCT images were optimized by selecting the "automatic all" function (Auto All), including the auto zooming function to set the appropriate position of the retina and the refraction focus, auto focusing function to set the appropriate focus for each patient's refraction, and auto polarizing function to optimize the image for each patient's polarization.

Microvascular information was quantitatively expressed as MVD (%). The proportion of the retinal area occupied by blood vessels was automatically calculated and defined as the MVD. Blood vessels with flow were defined by pixels with decorrelation values above the split-spectrum amplitude-decorrelation angiography threshold level. The microvasculature at different retinal layers was segmented and visualized as previously described.[17] MVDs were determined on full-thickness 3 × 3-mm OCT retinal scans, centered on the fovea (Fig. 2D). The images were automatically segmented into the inner retina (Fig. 2E), the SCP (Figs. 2F, 2G), and the DCP (Figs. 2H, 2I) with some manual adjustments by two investigators before calculating the MVD. Whole-image vessel density was measured over the entire scan field. Parafoveal MVD was further calculated in the area encompassed by a 0.5- to 1.5-mm radius (Figs. 2G, 2I). To match the area with the AO image, the raw OCTA images were exported and further analyzed by a custom automated algorithm as described previously.[33,36]

Intersession Repeatability

Twenty-three normal subjects were imaged on two separate occasions in 1 year. The repeatability of the CD measurements in each local region and in the TAZ between two imaging sessions was evaluated by calculating the intraclass correlation coefficient and the coefficient of repeatability percentage for each subject.[29,37] Bland-Altman plots were also used to assess the agreement between the two repeated measurements.

Statistical Analysis

Statistical analyses were performed using the Statistical Package for Social Sciences (version 20.0; SPSS, Inc., Chicago, IL, USA). All quantitative variables were summarized as means and standard deviations, and qualitative variables were summarized as frequencies or percentages. BCVA was expressed as the logarithm of the minimum angle of resolution (logMAR). Variable normality was inspected by using histograms and the Shapiro-Wilk test. One-way analysis of variance (ANOVA) was used to compare the differences among the three groups, and post hoc procedures were used to compare differences between groups. The generalized estimating equation was used to compare the CD and MVD measurements among the groups, accounting for the intrasubject correlations caused by using both eyes from the same subject. The Spearman correlation was used to assess the relationships among CD, MVD, and logMAR visual acuity. *P* values of less than 0.05 were considered statistically significant.

Results

Demographics and Genetics

Thirty-seven eyes from 20 patients with RP (age, 32 ± 14.8 years; range, 7 to 60 years) and 54 eyes from 29 age-matched

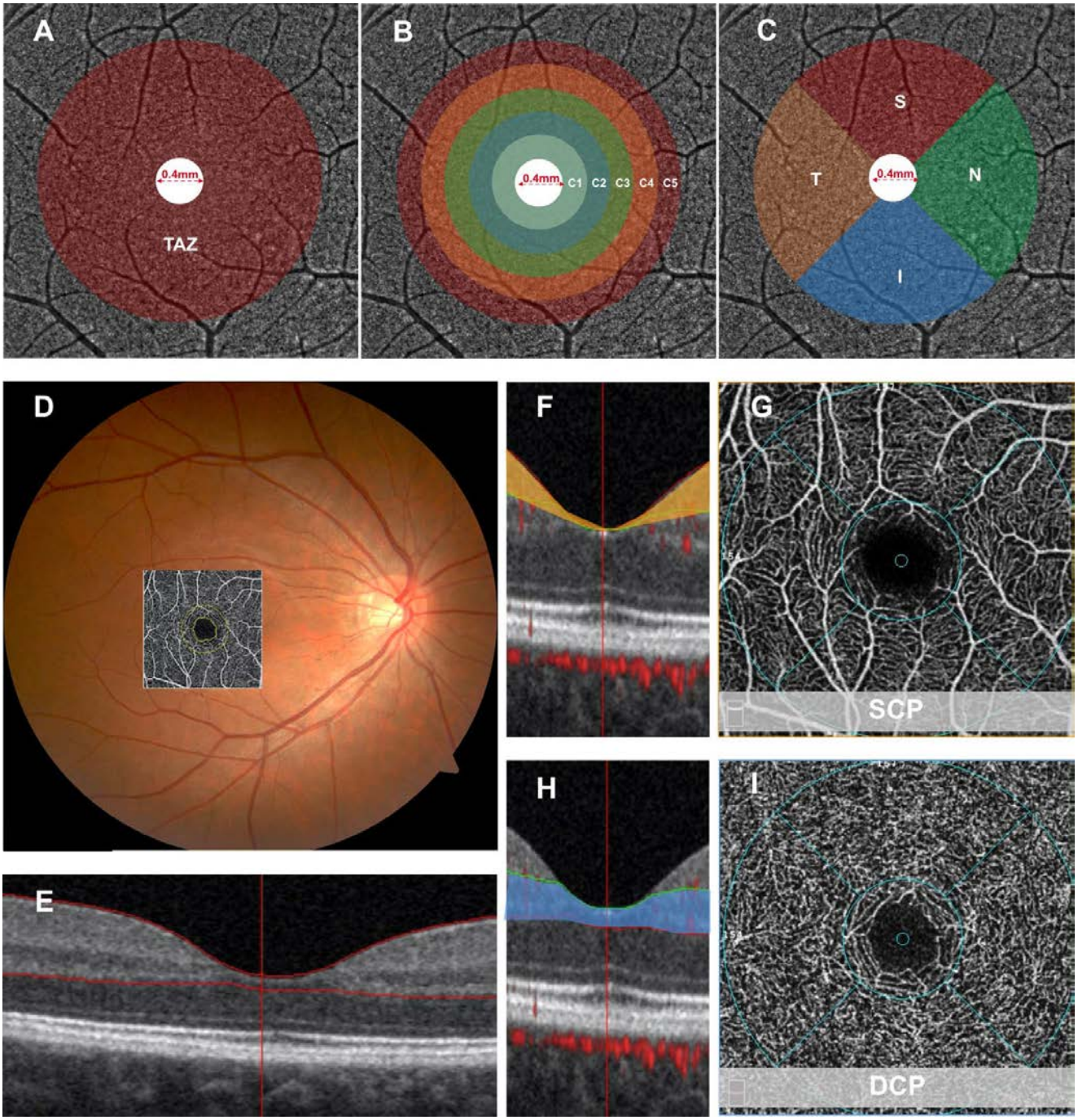

Figure 2. Analysis regions of a normal eye for assessing CD by AO and vascular segmentation by OCTA. (**A**) Analyses of the mCD in the TAZ with a diameter of 2.4 mm after excluding the central area (diameter, 0.4 mm). (**B**) Analyses of CD with fixed spacing (0.2 mm) in five concentric rings: C1 (diameter, 0.8 mm), C2 (diameter, 1.2 mm), C3 (diameter, 1.6 mm), C4 (diameter, 2.0 mm), and C5 (diameter, 2.4 mm). (**C**) Analysis of CD in four parafoveal quadrant sectors: T, S, N, and I. (**D**) Retinal OCTA scan area of 3×3 mm superimposed over a fundoscopy image of the same eye. (**E**) B-scan image of the inner retina (outlined in *red*). (**F**) B-scan image of superficial layer segmentation (*yellow*). (**G**) Vessels of the SCP. (**H**) B-scan image of deep layer segmentation (*blue*). (**I**) Vessels of the DCP.

healthy participants (age, 32.4 ± 11.6 years; range, 21 to 67 years) were included in this study. There were no significant differences in age among the control and two RP groups (ANOVA, $P = 0.979$; Table 1). All of the RP patients were assigned to either the moderate or severe groups based on the EZ width. The EZ width was 2859 ± 1284 μm and 1154 ± 207.47 μm in the moderate and severe RP group, respectively. There were significant differences in BCVA and AL among the three groups (ANOVA, $P < 0.001$).

Based on the genetic mutations (Supplementary Table S1), the inheritance patterns were identifiable in all patients. Genetic testing was performed in all 20 RP patients from 19 Chinese families that were unrelated to one another, and genotypes were identified in 11 patients (55%). Mutations in *RPGR*, *RP2*, *USH2A*, *EYS*, and *OFD1* were identified. Various patterns of RP and stages of degeneration were present in our cohort (Table 2).

Table 1. Summary of RP Patient and Normal Control Characteristics

Characteristic	Control	RP Moderate	RP Severe
Number of eyes	54	17	20
Age, y	32.44 ± 11.57	28.47 ± 15.96	32.16 ± 12.64
EZ width, μm	NA	2859 ± 1284	1154 ± 207.4
BCVA, logMAR	−0.02 ± 0.04	0.22 ± 0.13	0.43 ± 0.23
AL, mm	24.29 ± 1.21	23.12 ± 0.74	23.28 ± 0.74

Data are the means ± standard deviations. NA, not applicable.

Repeatability of CD Measurements

The CD repeatability in the TAZ averaged 1173 cones/mm^2 (Supplementary Table S2), equivalent to 6.7% of the average CD. This means that the difference between two measurements for the same subject would be less than the repeatability value of 1173 cones/mm^2 for 95% of pairs of observations. For the two repeated measurements, the intraclass correlation coefficient for the CD varied from 0.911 to 0.966 (Supplementary Table S2). Bland-Altman analysis showed that the difference between the two repeated measurements of the CD in the normal group was within the limits of agreement at each local region and the TAZ (Supplementary Fig. S2).

Comparison of CD and MVD Among RP Groups and Controls

In RP patients, 37 out of 40 eyes were successfully imaged (Fig. 3). Three eyes of 3 RP patients were excluded because of the low quality of the AO camera images. For all other eyes, CD was calculated in the 5 concentric rings (C1–C5), 4 quadrants (I, N, S, and T), and the TAZ.

For the moderate RP group, the mCDs in C2 and C3 were significantly lower than in the control group ($P < 0.001$, $P = 0.005$, respectively) but not for C1, C4, and C5. The mCDs in TAZ and the four quadrants were not significantly different from the control group (Table 3; Fig. 4A).

For the severe RP group, the mCDs for C1 to C5 were each significantly lower than in the control group and the moderate RP group ($P < 0.001$ for each concentric ring, respectively; Table 3; Fig. 4B). The mCD in the TAZ and the four quadrants were also significantly lower than in the control group and moderate RP group. Although we undertook an analysis to evaluate cone densities based on retinal eccentricity, there were no apparent quadrant effects on mCDs (data not shown).

MVD in the concentric rings (C1–C5) were analyzed subsequently. In the moderate RP group, the MVDs of C2 to C5 in the SCP were significantly lower than those in the control group ($P < 0.05$) but not in C1. Furthermore, the MVDs of C1 to C5 in the DCP were significantly lower than in the control group ($P < 0.01$; Fig. 4C). Starting from the second ring, the moderate and severe RP groups demonstrated progressively decreasing MVDs with increasing eccentricity, in line with the trend of changes in CD.

Retinal flow areas (0.5- to 1.5-mm radius) were measured by the internal software of the instrument. For both moderate and severe RP groups, the MVDs were significantly lower than in the control group for both the SCP and DCP ($P < 0.05$; Table 4). However, in the severe RP group, the value of vascular loss was more noticeable in the DCP.

AO images revealed a distinct mosaic pattern of RPE cells in regions where cones appeared to be missing. In all normal eyes, a well-defined cone photoreceptor mosaic pattern was present (Figs. 5A–D). In 10 eyes of RP patients (27%), the cone loss was clearly evident in the AO images, and the cone photoreceptor mosaic pattern was abnormal. In a representative AO montage image (patient P19; Figs. 5E–H), the cones were spread sparsely throughout the region.

Correlation Analysis

In RP patients, there is a significant correlation between EZ width and the mCD in the TAZ ($r = 0.74$, $P < 0.001$; Fig. 6A). The mCD of the TAZ correlated with logMAR BCVA ($r = -0.52$, $P = 0.002$; Fig. 6B). Additionally, the mCD for concentric ring

Table 2. Demographics and Clinical Characteristics of RP Patients

				BCVA, logMAR		Spherical Equivalent, D		AL, mm	
Patient/Family	Age*, y/Sex	Mutation	Inheritance	OD	OS	OD	OS	OD	OS
P1/F1	30/F	RPGR	XLRP	0.4	0.2	−3.75	−4.25	23.8	23.8
P2/F1	7/M	RPGR	XLRP	0.3	0.3	−0.25	−0.50	22.11	22.15
P3/F2	29/M	EYS	Simplex RP	0.3	0.3	−0.50	−0.50	23.91	23.85
P4/F3	33/M	USH2A	Simplex RP	0.15	0.1	−2.00	−2.50	22.2	22.31
P5/F4	24/M	N/A	Simplex RP	0.22	0.5	0.75	0.50	22.86	22.29
P6/F5	60/M	N/A	Simplex RP	0.5	0.3	−3.00	−1.00	24.58	23.37
P7/F6	45/F	USH2A	Simplex RP	0.4	0.4	0.25	0.50	22.41	22.51
P8/F7	56/M	USH2A	Simplex RP	0.3	0.3	1.00	1.38	22.72	22.67
P9/F8	39/M	OFD1	XLRP	1.3	0.8	0.13	0.25	23.14	22.90
P10/F9	39/F	N/A	ADRP	0.8	0.5	−2.25	−2.75	NA	23.52
P11/F10	11/M	N/A	Simplex RP	0.3	0.2	−1.25	−1.25	23.44	23.28
P12/F11	9/M	RP2	XLRP	0.7	0.7	−3.75	−3.25	24.62	24.32
P13/F12	27/M	RPGR	XLRP	0.4	0.4	−2.50	−2.50	24.06	24.03
P14/F13	32/M	N/A	Simplex RP	0.22	0.3	−1.25	−2.75	22.17	22.19
P15/F14	42/M	N/A	Simplex RP	0.22	0.2	−1.00	−1.00	22.42	22.21
P16/F15	26/M	OFD1	XLRP	0.1	0.2	−1.00	−3.00	22.56	22.71
P17/F16	36/F	N/A	Simplex RP	0.05	0.0	−2.75	−2.75	23.57	23.35
P18/F17	48/M	N/A	Simplex RP	0.7	0.7	1.00	0.75	22.48	22.54
P19/F18	16/M	RPGR	XLRP	0.22	0.3	−0.75	−2.00	22.73	22.73
P20/F19	28/M	N/A	Simplex RP	0.1	0.1	−0.75	−1.00	23.45	23.38

F, female; M, male; N/A, not available; D, diopters; ADRP, autosomal dominant RP; XLRP, X-linked RP.
* Age at visit.

Investigative Ophthalmology & Visual Science

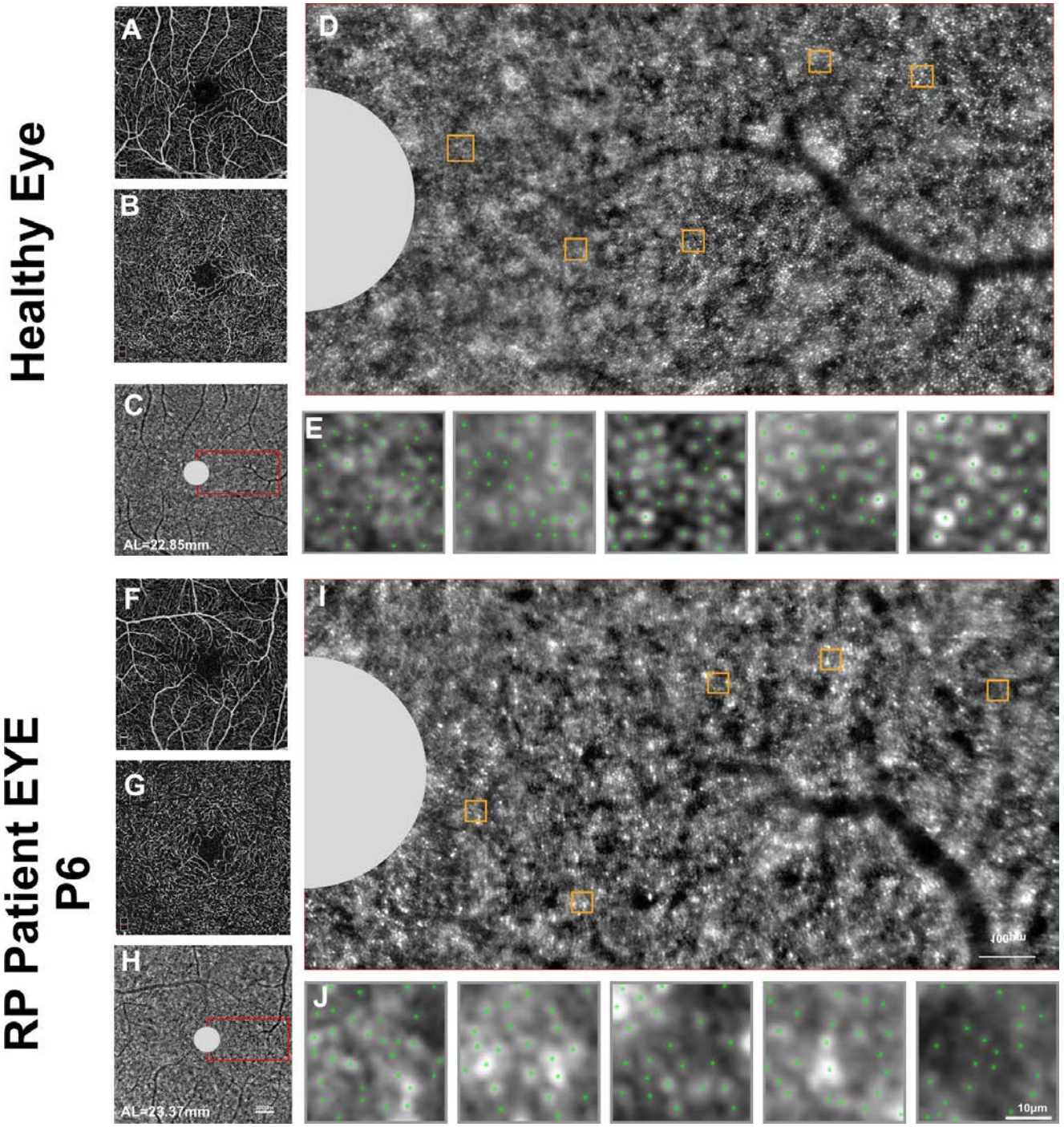

FIGURE 3. Representative OCTA images, AO montage images, and magnified images in a healthy eye and in a moderate RP eye from patient P6. The images were acquired in 3 × 3-mm areas around the fovea. OCTA scans of the retinal vasculature: (**A**, **F**) SCP and (**B**, **G**) DCP. (**C**, **H**) AO montage images with *red rectangular boxes* showing regions of interest (**D**, **I**). From within the regions of interest (**D**, **I**), selected areas were magnified (insets **E**, **J**) that corresponded with same area having identifiable cones.

C1 was not correlated with logMAR BCVA ($P = 0.054$), but the mCDs in concentric rings C2 to C5 were each negatively correlated with it ($P \leq 0.012$ for each concentric ring; Table 5). There were no significant correlations between the MVD in the SCP or DCP with logMAR BCVA (Table 5). The mCD was correlated with the MVD in the DCP (r = 0.43; $P = 0.028$; Fig. 6C, 6D) but not with the MVD in the SCP (r = –0.19, $P = 0.323$).

DISCUSSION

In this cross-sectional study, we used high-resolution imaging methods to investigate the distribution of CD and the microvascular structure in eyes with RP. Overall, we found that RP patients were characterized by decreases in both CD and MVD. In the DCP, there a positive correlation between CD and MVD but not in the SCP.

Table 3. CD in the Concentric Rings, TAZ, and Parafoveal Quadrants

Zone	Control ($N = 54$)	RP Moderate ($N = 17$)	RP Severe ($N = 21$)	Control vs. Moderate		Control vs. Severe		Moderate vs. Severe	
				% Difference	*P* Value	% Difference	*P* Value	% Difference	*P* Value
C1	23,691 ± 2,941	22,726 ± 2,648	16,338 ± 4,139	−4.1	0.96	−31.0	**<0.001**	−28.1	**<0.001**
C2	23,278 ± 2,776	19,885 ± 2,427	14,751 ± 3,089	−14.6	**<0.001**	−36.6	**<0.001**	−25.8	**<0.001**
C3	20,974 ± 2,074	18,741 ± 2,317	14,091 ± 2,863	−10.6	**0.005**	−32.8	**<0.001**	−24.8	**<0.001**
C4	18,734 ± 1,460	18,086 ± 2,086	13,794 ± 3,030	−3.5	0.86	−26.4	**<0.001**	−23.7	**<0.001**
C5	17,247 ± 1,327	17,473 ± 2,084	13,428 ± 3,034	1.3	1.00	−22.1	**<0.001**	−23.2	**<0.001**
TAZ	19,888 ± 1,647	18,733 ± 2,117	14,139 ± 2,856	−5.8	0.19	−28.9	**<0.001**	−24.5	**<0.001**
I	19,739 ± 1,964	18,737 ± 2,371	13,543 ± 3,091	−5.1	0.46	−31.4	**<0.001**	−27.7	**<0.001**
N	20,305 ± 1,936	18,744 ± 2,005	13,671 ± 3,538	−7.7	0.10	−32.7	**<0.001**	−27.1	**<0.001**
S	18,871 ± 1,673	17,997 ± 2,392	14,397 ± 3,167	−4.6	0.57	−23.7	**<0.001**	−20.0	**<0.001**
T	20,573 ± 1,945	19,397 ± 2,667	14,868 ± 3,339	−5.7	0.33	−27.7	**<0.001**	−23.4	**<0.001**

CD reported as cells/mm^2; values are means ± standard deviations of cells/mm^2. Statistical significance tested by ANOVA and adjusted for multiple comparisons using the Holm-Bonferroni method. Significant *P* values < 0.05 are shown in bold.

Previous studies assessed CD and spacing by using a small sampling window size.[38–41] Here, we evaluated CD over a much larger window, dividing the parafoveal area into concentric rings and quadrant sectors. With this approach, we were able to reliably evaluate CD and differences in cone distribution between normal eyes and eyes with moderate and severe RP. The CD that we found in normal eyes was similar to those in previous studies (Fig. 7).[29,42,43] However, the published values for CD vary widely, probably due to the large interindividual variability and the different sampling methods. Feng et al.[29] illustrated one region of interest could produce a range of CD measurements depending on the size and placement of the sampling window.

In the overall assessment of photoreceptor changes, we found a significant decrease in the CD of the TAZ in the severe RP group but not in the moderate RP group. Upon further analysis of the moderate RP group, the mCD was significantly decreased in areas C2 and C3 but not in C5. The mCD in areas C1 and C4 also decreased, but the changes were not statistically significant. This is somewhat consistent with a previous report by Miyata et al.[23] who found a reduction in CD at 0.5 mm from the center of the fovea but not at 1.0 mm in RP patients. However, the magnitude of cone loss was significantly greater in C2 (400–600 μm from the foveal center) in both the moderate and severe RP group (−14.6% and −36.6%, respectively). This may indicate that the greatest amount of cone degeneration occurs in this area. One possible explanation for this is the codependence between rods and cones. Rod cells produce a factor, rod-derived cone viability factor, that increases the survival of cones cells.[44,45] Therefore, as rod photoreceptor death progresses, cone death may follow as a secondary effect due to the loss of rod-derived cone viability factor support. However, in histologic data, Curcio et al.[43] reported that the CD was equal with the rod density at about 400 to 500 μm (1.5 degree) from the center of the fovea (Fig. 7). Thus, it is still not certain if the loss of rods in C2 is the cause of the biggest loss of CD. The rod photoreceptor is too small for the flood-illumination AO camera to identify. However, with AOSLO, which can image rod cells, we may be able to elucidate the mechanism of secondary cone degeneration by visualizing rods.

In our AO images, RPE-like structures were visible in the dark regions of the retina in some RP patients. Previous studies showed that the waveguide properties of cone outer segments prevent the visibility of RPE structure.[46,47] Sun et al.[39] found that reduced CD in Usher syndrome was a result of a reduced number of normal waveguiding cones. They hypothesized that the findings were due to the different molecular pathways involved in RP versus Usher syndrome. For example, changes in outer segment proteins may not impact cone waveguiding as much as changes in proteins localized to the connecting cilium. Thus, it is likely that different forms of RP would have different effects on cone survival and CD, and each could affect the visibility of the RPE in different ways.

We also used projection-resolved OCTA to characterize changes in the microvasculature of RP patients. Projection artifacts of the deeper layer occur due to fluctuating shadows cast by flowing blood in a superficial layer. With the use of this algorithm, the measurements in the deep network more precisely represent the actual flow there. Moreover, to ensure

Table 4. Microvascular Measurements in RP and Healthy Eyes

Parameter	Control, % ($N = 54$)	RP Moderate, % ($N = 17$)	RP Severe, % ($N = 21$)	Control vs. Moderate		Control vs. Severe		Moderate vs. Severe	
				% Change	*P* Value	% Change	*P* Value	% Change	*P* Value
SCP MVD,									
wiMVD	45.37 ± 3.64	40.22 ± 3.58	39.18 ± 4.51	−11.36	**<0.001**	−13.64	**<0.001**	−2.57	1.00
pfMVD	48.95 ± 3.73	41.83 ± 4.56	41.64 ± 4.93	−14.55	**<0.001**	−14.95	**<0.001**	−0.46	1.00
DCP MVD									
wiMVD	50.4 ± 3.41	45.33 ± 8.89	38.52 ± 8.77	−10.06	**0.019**	−23.57	**<0.001**	−15.03	**0.005**
pfMVD	52.84 ± 3.4	47.7 ± 9.44	39.58 ± 9.46	−9.73	**0.026**	−25.10	**<0.001**	−17.04	**0.001**
Custom Interval of MVD (radii, mm)									
SCP (0.2–1.2)	41.85 ± 1.92	38.85 ± 2.29	39.37 ± 3.80	−7.17	**0.001**	−5.92	**0.004**	1.34	1.00
DCP (0.2–1.2)	54.21 ± 1.71	42.3 ± 5.65	35.9 ± 6.45	−21.96	**<0.001**	−33.77	**<0.001**	−15.13	**<0.001**

MVD reported as the proportion (%) of the retinal area occupied by blood vessels. Values are means ± standard deviations. Statistical significance tested by ANOVA and adjusted for multiple comparisons using the Holm-Bonferroni method. wiMVD, whole image MVD; pfMVD, parafoveal MVD. Significant *P* values < 0.05 are shown in bold.

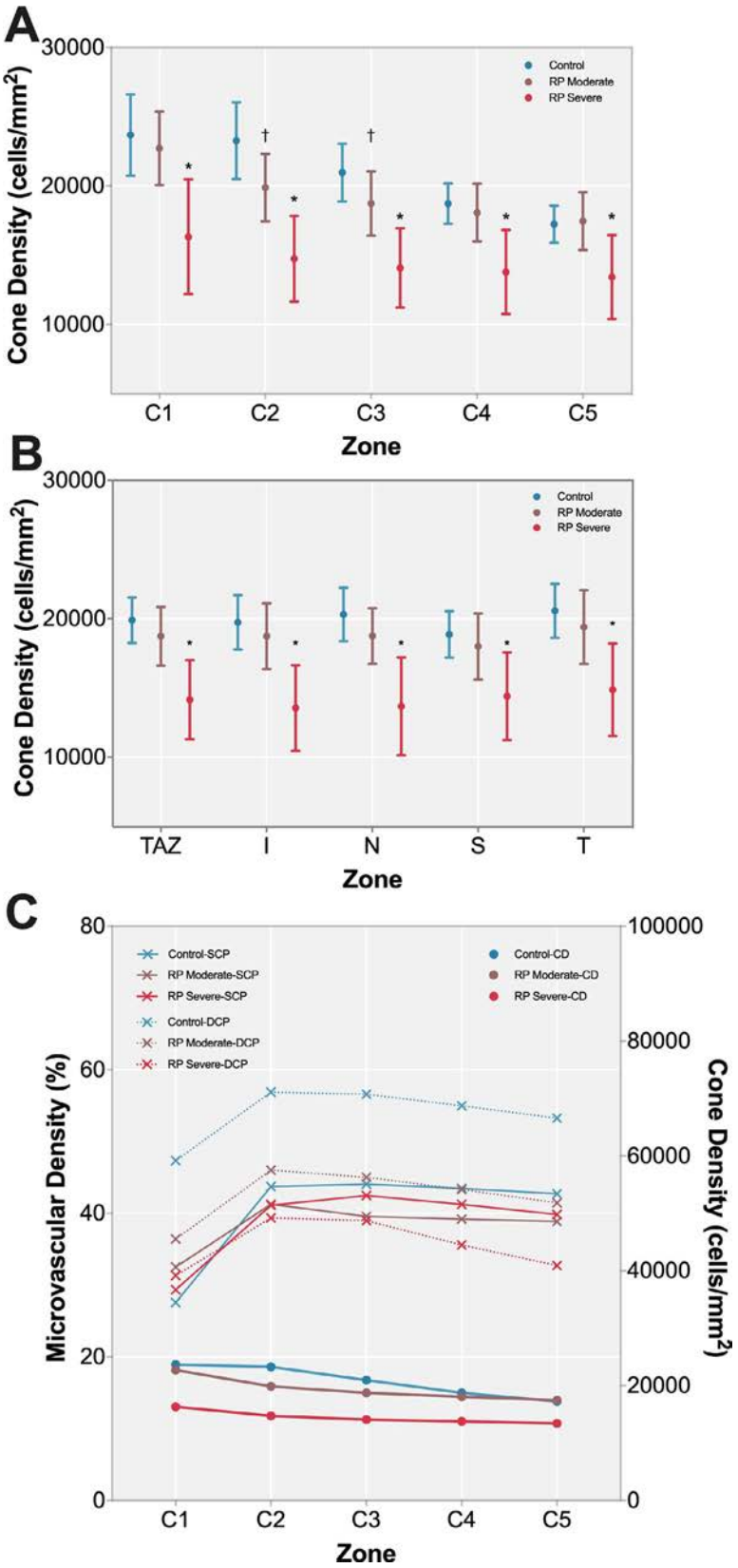

Figure 4. Comparison of CDs and MVD among control and RP groups. (**A**) CDs are shown for each concentric ring. (**B**) CDs for the TAZ and four quadrant sectors. (**C**) MVDs and CDs shown in the concentric rings. MVD, the *y*-axis on the left. The *y*-axis on the right, CD. †$P < 0.05$, the CDs in the moderate group were lower than that in the control group; *$P < 0.001$, the CDs in the severe RP group were lower than that in the control group.

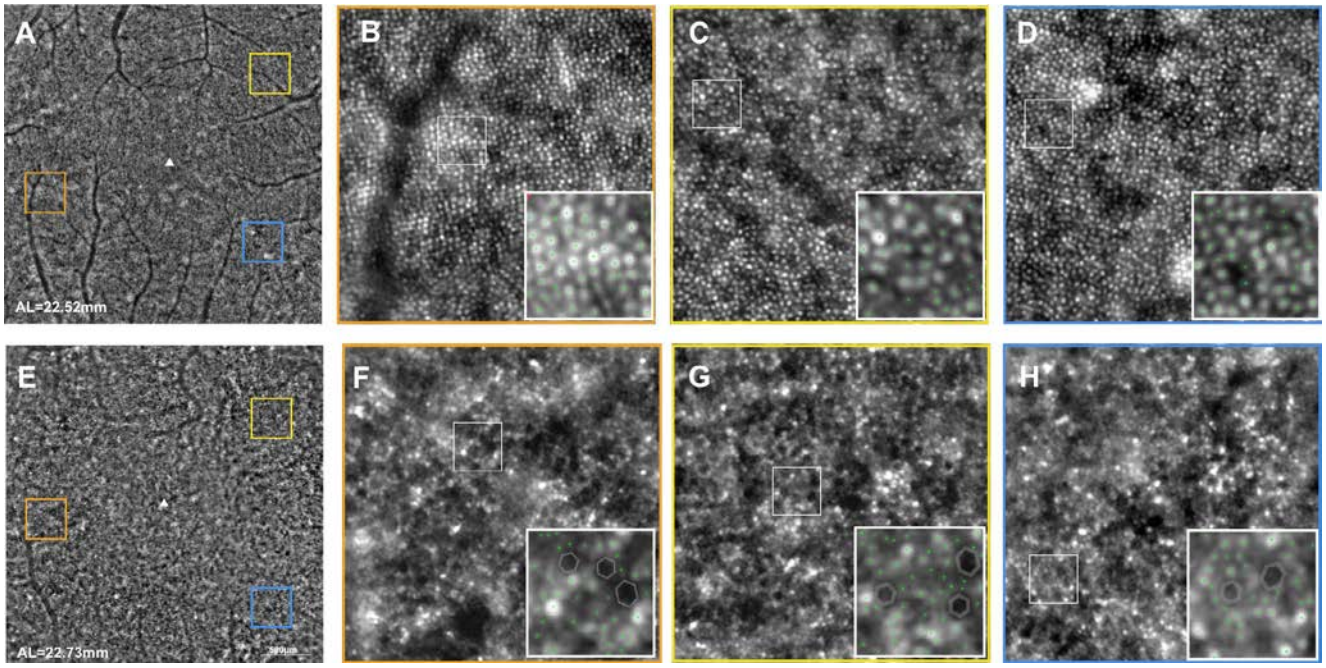

Figure 5. Adaptive optics (AO) images of an age-matched normal subject and a RP patient with mutation in RPGR. (**A**) Central 10° AO image of normal subject. Magnified images and cones identified within the *orange*, *yellow*, and *blue squares* in (**B**), (**C**), and (**D**), respectively. (**E**) Central 10° AO image of moderate RP patient P19. Magnified images and cones identified within the *orange*, *yellow*, and *blue squares* are shown in (**F**), (**G**), and (**H**), respectively. The hexagon-shaped RPE-like cells have been outlined. Compared to the corresponding locations in normal subjects, these areas reveal severe disruption of the cone mosaic. The RPE-like mosaic structure can be clearly observed below sporadic bright cones.

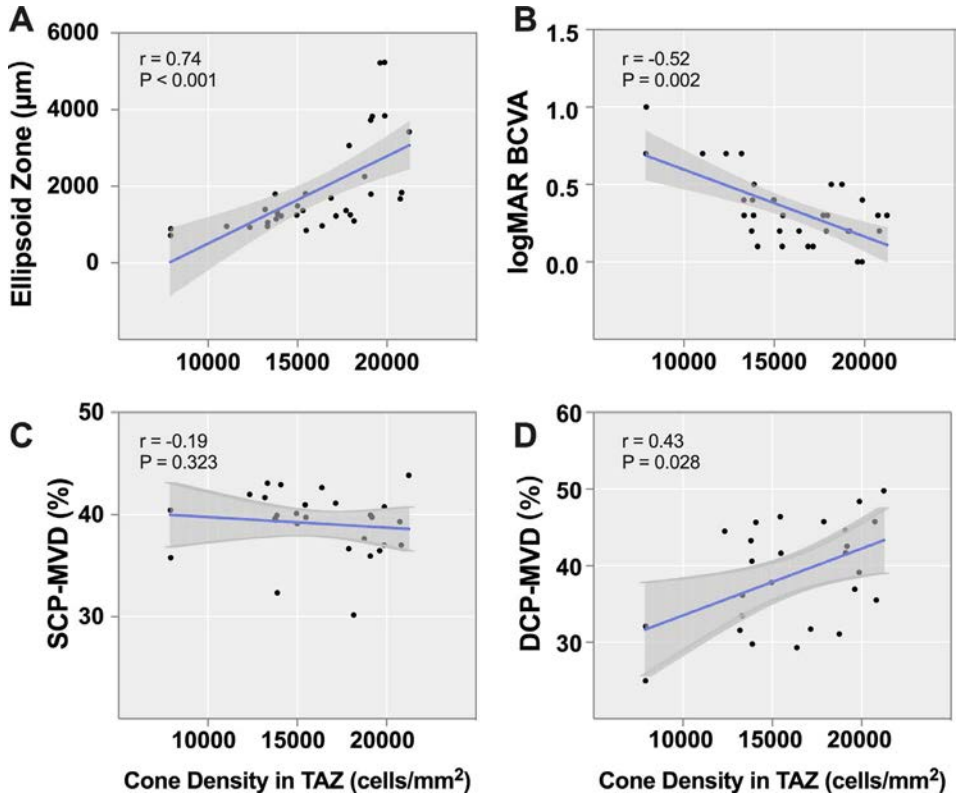

Figure 6. Scatterplots illustrating the correlation between the mCD in the TAZ and EZ width (**A**), logMAR BCVA (**B**), and the microvasculature density in the SCP (**C**) and the DCP (**D**). The *dashed lines* are the 95% confidence intervals for the *solid trend lines*.

Investigative Ophthalmology & Visual Science

Table 5. Correlation Among BCVA, CD, and MVD in All Eyes

Parameter	r	P
logMAR BCVA		
CD		
C1	−0.33	0.054
C2	−0.43	**0.012**
C3	−0.52	**0.002**
C4	−0.50	**0.002**
C5	−0.52	**0.002**
TAZ	−0.52	**0.002**
MVD		
wiMVD in SCP	−0.13	0.455
pfMVD in SCP	0.04	0.826
wiMVD in DCP	−0.03	0.847
pfMVD in DCP	−0.03	0.858
TAZ in SCP	−0.06	0.747
TAZ in DCP	−0.30	0.132
CD in TAZ		
EZ	**0.74**	**<0.001**
MVD		
TAZ in SCP	−0.19	0.323
TAZ in DCP	0.43	**0.028**

Significant P values < 0.05 are shown in bold.

accuracy of the MVD, each layer of the alignment was corrected manually. In our current study, the MVDs in both SCP and DCP were significantly reduced in RP. These findings agree with previous work demonstrating significant differences in the MVD of both the superficial and deep networks.[16,18,48]

The vascular supply for the outer retina is delivered by the vessels in the choroid, and the inner retina is supplied by the retinal vasculature.[49] Rods cells, which have a very high metabolic rate, constitute 95% of the cells in the outer nuclear layer. The loss of rod cells in RP will dramatically reduce oxygen consumption in the outer retina. Consequently, the level of oxygen in the outer retina will increase following the death of the rod cells.[50] In experimental models, the resulting high level of oxygen spills over from the outer retina to the inner retina. In a cat model of RP,[51] the loss of photoreceptor metabolism allowed choroidal oxygen to reach the inner retina, causing attenuation of the retinal circulation. In the current study, we found that the CD was correlated with MVD in the DCP. Based on these results, we suspect that the deep retinal vasculature is more vulnerable than might be expected to alterations in severe RP.

It is possible that decreased blood flow accelerates the late phase of retinal degeneration. A recent experimental study showed that neurovascular crosstalk between interneurons and capillaries is required for vision.[52] There will be profound effects on photoreceptor survival and function with the loss of this crosstalk. Other studies also found that dying photoreceptors in mouse models of RP exhibited molecular and morphologic characteristics of nutrient starvation.[53,54] These findings suggest that decreased blood flow may stress the cone cells in RP. In the current study, we could not determine if the loss of CD or loss of MVD in RP was the dominant disease process. Further studies are needed to collect longitudinal follow-up data in RP patients.

Currently, some therapeutic options for RP are showing promising results, for example, stem cells and gene therapy.[55] As these therapies are considered for clinical application, the evaluation of treatment outcomes are among some of the issues that must be addressed. The present study revealed significant correlations between CD in the area of parafovea and visual acuity. The correlations demonstrated that CD may play an important role in normal visual acuity, and reducing or eliminating CD loss may be essential in retaining vision. However, CD in C1 was not correlated with the visual acuity, which suggests that the degrees of reduction in these two parameters were different. Thus, visual acuity might not be a sensitive indicator of RP prior to structural loss. In a previous report, Ratnam et al.[38] proposed that objective measures of cone structure might be more sensitive indicators of disease severity than visual acuity. That information may guide posttreatment evaluation in the future. Talcott et al.[56] used AO technologies to evaluate the RP progression and response to an experimental treatment for retinal degeneration.[57] Although it may not be sufficient to assess whether or not a treatment is effective, AO technology will likely contribute to faster and more cost effective drug development for the treatment of eye diseases.

This is the first time we evaluated CD over a much larger window in normal and RP patients, and there are some limitations in the method that may have affected the results. One limitation is that the accuracy of CD estimation within such a large area, namely, 0.4- to 2.4-mm diameter, might be reduced by the low quality of measurements in certain areas. However, the high repeatability of measurements ensures that this algorithm has sufficient precision. When we compared the CDs in the RP and normal groups, the differences were within

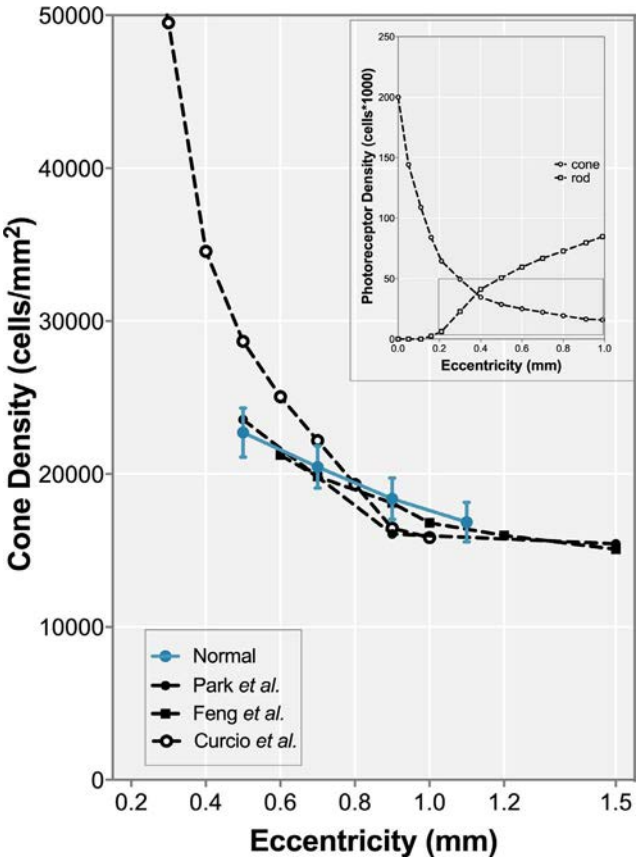

Figure 7. Comparison of literature values for cone and rod densities as a function of distance from the fovea in normal eyes. The curves in the inset show Curcio's data for the distribution of rods and cones, which are at equal density at 400 to 500 μm C2 from the foveal center.[43] The *blue solid curve* is our AO data acquired from normal eyes. *Error bars* represent the confidence interval (± 2 standard deviations). The data by Curcio et al.[42] were determined by histology. The data by Park et al.[42] were acquired by AOSLO. The data by Feng et al.[29] were acquired by AO.

the normal variation in repeatability studies. Thus, this algorithm can reliably detect the CD in the RP groups. Although there were some abnormally hyperreflective spots in the AO images, we manually checked for the presence of these and eliminated any that were present.

Another limitation of this study is that of the resolution of the AO images. The resolution of the rtx1 AO fundus camera was 4 μm, which is insufficient to measure the high packing density at the foveola. We did find correlations between mCD and visual acuity in parafoveal zones, and this reflects the impairment of visual function caused by the structure changes. However, a crucial factor affecting visual acuity is the high density of cones in the foveal centralis.[58] This technical limitation of the AO fundus camera could be overcome with the development of a new generation AOSLO or improvements in the AO camera.

Finally, our data do not explain the relationship between the genetic heterogeneity and severity of disease. One reason for this is that RP is an inherited retinal degenerative disease that has been associated with more than 80 gene mutations, each of which may affect rod and cone survival differently.[59] Due to the limitation of sample size, we were not able to draw clear conclusions with regard to specific mutations and disease severity. Future studies may add more information regarding the RP subsets and disease onset and progression.

Our study compared CD and MVD in corresponding regions of normal and RP eyes. Decreased CD and MVD were present in both moderate and severe RP groups. In addition, cone loss was accompanied by significant changes in the DCP. In conclusion, our results demonstrated that quantitative changes are meaningful in assessing the pathophysiology of RP.

Acknowledgments

Supported by Natural Science Foundation of China (81600772, 81970838, and 81790644), National Key Research and Development Program of China (2017YFA0105300), Zhejiang Provincial Natural Science Foundation of China (LD18H120001), and the Ministry of Education 111 Project (D16011). The authors have no proprietary interest in any materials or methods described in this article.

Disclosure: **R. Lin**, None; **M. Shen**, None; **D. Pan**, None; **S.-Z. Xu**, None; **R.-J. Shen**, None; **Y. Shao**, None; **C. Shi**, None; **F. Lu**, None; **Z.-B. Jin**, None

References

1. Hartong DT, Berson EL, Dryja TP. Retinitis pigmentosa. *Lancet*. 2006;368:1795–1809.
2. Milam AH, Li ZY, Fariss RN. Histopathology of the human retina in retinitis pigmentosa. *Prog Retin Eye Res*. 1998;17:175–205.
3. Dias MF, Joo K, Kemp JA, et al. Molecular genetics and emerging therapies for retinitis pigmentosa: basic research and clinical perspectives. *Prog Retin Eye Res*. 2018;63:107–131.
4. Jones BW, Pfeiffer RL, Ferrell WD, Watt CB, Marmor M, Marc RE. Retinal remodeling in human retinitis pigmentosa. *Exp Eye Res*. 2016;150:149–165.
5. Stone JL, Barlow WE, Humayun MS, de Juan E Jr, Milam AH. Morphometric analysis of macular photoreceptors and ganglion cells in retinas with retinitis pigmentosa. *Arch Ophthalmol*. 1992;110:1634–1639.
6. Grunwald JE, Maguire AM, Dupont J. Retinal hemodynamics in retinitis pigmentosa. *Am J Ophthalmol*. 1996;122:502–508.
7. Cellini M, Strobbe E, Gizzi C, Campos EC. ET-1 plasma levels and ocular blood flow in retinitis pigmentosa. *Can J Physiol Pharmacol*. 2010;88:630–635.
8. Aizawa S, Mitamura Y, Baba T, Hagiwara A, Ogata K, Yamamoto S. Correlation between visual function and photoreceptor inner/outer segment junction in patients with retinitis pigmentosa. *Eye (London)*. 2009;23:304–308.
9. De Rojas JO, Schuerch K, Mathews PM, et al. Evaluating structural progression of retinitis pigmentosa after cataract surgery. *Am J Ophthalmol*. 2017;180:117–123.
10. Hood DC, Lazow MA, Locke KG, Greenstein VC, Birch DG. The transition zone between healthy and diseased retina in patients with retinitis pigmentosa. *Invest Ophthalmol Vis Sci*. 2011;52:101–108.
11. Campochiaro PA, Mir TA. The mechanism of cone cell death in retinitis pigmentosa. *Prog Retin Eye Res*. 2018;62:24–37.
12. Liang J, Williams DR. Aberrations and retinal image quality of the normal human eye. *J Opt Soc Am A Opt Image Sci Vis*. 1997;14:2873–2883.
13. Roorda A, Romero-Borja F, Donnelly WJ III, Queener H, Hebert T, Campbell M. Adaptive optics scanning laser ophthalmoscopy. *Opt Express*. 2002;10:405–412.
14. Kashani AH, Chen CL, Gahm JK, et al. Optical coherence tomography angiography: a comprehensive review of current methods and clinical applications. *Prog Retin Eye Res*. 2017;60:66–100.
15. Chen CL, Wang RK. Optical coherence tomography based angiography [Invited]. *Biomed Opt Express*. 2017;8:1056–1082.
16. Battaglia Parodi M, Cicinelli MV, Rabiolo A, et al. Vessel density analysis in patients with retinitis pigmentosa by means of optical coherence tomography angiography. *Br J Ophthalmol*. 2017;101:428–432.
17. Koyanagi Y, Murakami Y, Funatsu J, et al. Optical coherence tomography angiography of the macular microvasculature changes in retinitis pigmentosa. *Acta Ophthalmol*. 2018;96:e59–e67.
18. Toto L, Borrelli E, Mastropasqua R, et al. Macular features in retinitis pigmentosa: correlations among ganglion cell complex thickness, capillary density, and macular function. *Invest Ophthalmol Vis Sci*. 2016;57:6360–6366.
19. McCulloch DL, Marmor MF, Brigell MG, et al. ISCEV standard for full-field clinical electroretinography (2015 update). *Doc Ophthalmol*. 2015;130:1–12.
20. Huang XF, Huang F, Wu KC, et al. Genotype-phenotype correlation and mutation spectrum in a large cohort of patients with inherited retinal dystrophy revealed by next-generation sequencing. *Genet Med*. 2015;17:271–278.
21. Huang XF, Xiang P, Chen J, et al. Targeted exome sequencing identified novel USH2A mutations in Usher syndrome families. *PLoS One*. 2013;8:e63832.
22. Li KY, Roorda A. Automated identification of cone photoreceptors in adaptive optics retinal images. *J Opt Soc Am A Opt Image Sci Vis*. 2007;24:1358–1363.
23. Miyata M, Ooto S, Ogino K, et al. Evaluation of photoreceptors in Bietti crystalline dystrophy with CYP4V2 mutations using aptive optics scanning laser ophthalmoscopy. *Am J Ophthalmol*. 2016;161:196–205.e1.
24. Kuan DT, Sawchuk AA, Strand TC, Chavel P. Adaptive noise smoothing filter for images with signal-dependent noise. *IEEE Trans Pattern Anal Mach Intell*. 1985;7:165–177.
25. Lindeberg T. Linear scale-space and related multi-scale representations. In: *Scale-Space Theory in Computer Vision*. Berlin, Germany: Springer. 1994;256:349–382.
26. Xue B, Choi SS, Doble N, Werner JS. Photoreceptor counting and montaging of en-face retinal images from an adaptive optics fundus camera. *J Opt Soc Am A Opt Image Sci Vis* 2007;24:1364–1372.
27. Liu X, Zhang Y, Dai Y. An automated algorithm for photoreceptors counting in adaptive optic retinal images (E-Abstract 84191Z). *Proc SPIE*. 2012;8419.

28. Bennett AG, Rudnicka AR, Edgar DF. Improvements on Littmann's method of determining the size of retinal features by fundus photography. *Graefes Arch Clin Exp Ophthalmol*. 1994;232:361–367.
29. Feng S, Gale MJ, Fay JD, et al. Assessment of different sampling methods for measuring and representing macular cone density using flood-illuminated adaptive optics. *Invest Ophthalmol Vis Sci*. 2015;56:5751–5763.
30. Dabir S, Mangalesh S, Kumar KA, Kummelil MK, Sinha Roy A, Shetty R. Variations in the cone packing density with in emmetropes. *Eye (London)*. 2014;28:1488–1493.
31. Nakanishi A, Ueno S, Kawano K, et al. Pathologic changes of cone photoreceptors in eyes with occult macular dystrophy. *Invest Ophthalmol Vis Sci*. 2015;56:7243–7249.
32. Legras R, Gaudric A, Woog K. Distribution of cone density, spacing and arrangement in adult healthy retinas with adaptive optics flood illumination. *PLoS One* 2018;13: e0191141.
33. Chen Q, Ma Q, Wu C, et al. Macular vascular fractal dimension in the deep capillary layer as an early indicator of microvascular loss for retinopathy in type 2 diabetic patients. *Invest Ophthalmol Vis Sci*. 2017;58:3785–3794.
34. Jia Y, Tan O, Tokayer J, et al. Split-spectrum amplitude-decorrelation angiography with optical coherence tomography. *Opt Express*. 2012;20:4710.
35. Zhang M, Hwang TS, Campbell JP, et al. Projection-resolved optical coherence tomographic angiography. *Biomed Opt Express* 2016;7:816–828.
36. Kwapong WR, Peng C, He Z, Zhuang X, Shen M, Lu F. Altered macular microvasculature in neuromyelitis optica spectrum disorders. *Am J Ophthalmol*. 2018;192:47–55.
37. Garrioch R, Langlo C, Dubis AM, Cooper RF, Dubra A, Carroll J. Repeatability of in vivo parafoveal cone density and spacing measurements. *Optom Vis Sci*. 2012;89:632–643.
38. Ratnam K, Carroll J, Porco TC, Duncan JL, Roorda A. Relationship between foveal cone structure and clinical measures of visual function in patients with inherited retinal degenerations. *Invest Ophthalmol Vis Sci*. 2013;54:5836–5847.
39. Sun LW, Johnson RD, Langlo CS, et al. Assessing photoreceptor structure in retinitis pigmentosa and Usher syndrome. *Invest Ophthalmol Vis Sci*. 2016;57:2428–2442.
40. Choi SS, Doble N, Hardy JL, et al. In vivo imaging of the photoreceptor mosaic in retinal dystrophies and correlations with visual function. *Invest Ophthalmol Vis Sci* 2006;47: 2080–2092.
41. Makiyama Y, Ooto S, Hangai M, et al. Macular cone abnormalities in retinitis pigmentosa with preserved central vision using adaptive optics scanning laser ophthalmoscopy. *PLoS One*. 2013;8:e79447.
42. Park SP, Chung JK, Greenstein V, Tsang SH, Chang S. A study of factors affecting the human cone photoreceptor density measured by adaptive optics scanning laser ophthalmoscope. *Exp Eye Res*. 2013;108:1–9.
43. Curcio CA, Sloan KR, Kalina RE, Hendrickson AE. Human photoreceptor topography. *J Comp Neurol*. 1990;292:497–523.
44. Cepko C, Punzo C. Sugar for sight. *Nature*. 2015;522:428–429.
45. Léveillard T, Mohand-Saïd S, Lorentz O, et al. Identification and characterization of rod-derived cone viability factor. *Nat Genet*. 2004;36:755–759.
46. Scoles D, Sulai YN, Langlo CS, et al. In vivo imaging of human cone photoreceptor inner segments. *Invest Ophthalmol Vis Sci*. 2014;55:4244–4251.
47. Roorda A, Williams DR. Optical fiber properties of individual human cones. *J Vis*. 2002;2:404–412.
48. Rezaei KA, Zhang QQ, Chen CL, Chao J, Wang RK. Retinal and choroidal vascular features in patients with retinitis pigmentosa imaged by OCT based microangiography. *Graefes Arch Clin Exp Ophthalmol*. 2017;255:1287–1295.
49. Birol G, Wang S, Budzynski E, Wangsa-Wirawan ND, Linsenmeier RA. Oxygen distribution and consumption in the macaque retina. *Am J Physiol Heart Circ Physiol*. 2007;293: H1696–H1704.
50. Léveillard T, Sahel J-A. Metabolic and redox signaling in the retina. *Cell Mol Life Sci*. 2017;74:3649–3665.
51. Padnick-Silver L, Kang Derwent JJ, Giuliano E, Narfström K, Linsenmeier RA. Retinal oxygenation and oxygen metabolism in abyssinian cats with a hereditary retinal degeneration. *Invest Ophthalmol Vis Sci*. 2006;47:3683–3689.
52. Usui Y, Westenskow PD, Kurihara T, et al. Neurovascular crosstalk between interneurons and capillaries is required for vision. *J Clin Invest*. 2015;125:2335–2346.
53. Punzo C, Kornacker K, Cepko CL. Stimulation of the insulin/mTOR pathway delays cone death in a mouse model of retinitis pigmentosa. *Nat Neurosci*. 2009;12:44–52.
54. Murakami Y, Matsumoto H, Roh M, et al. Receptor interacting protein kinase mediates necrotic cone but not rod cell death in a mouse model of inherited degeneration. *Proc Natl Acad Sci U S A*. 2012;109:14598–14603.
55. Mandai M, Watanabe A, Kurimoto Y, et al. Autologous induced stem-cell-derived retinal cells for macular degeneration. *N Engl J Med*. 2017;376:1038–1046.
56. Talcott KE, Ratnam K, Sundquist SM, et al. Longitudinal study of cone photoreceptors during retinal degeneration and in response to ciliary neurotrophic factor treatment. *Invest Ophthalmol Vis Sci*. 2011;52:2219–2226.
57. Jin ZB, Gao ML, Deng WL, et al. Stemming retinal regeneration with pluripotent stem cells. *Prog Retin Eye Res*. 2019;69:38–56.
58. Provis JM, Dubis AM, Maddess T, Carroll J. Adaptation of the central retina for high acuity vision: cones, the fovea and the avascular zone. *Prog Retin Eye Res*. 2013;35:63–81.
59. Verbakel SK, van Huet RAC, Boon CJF, et al. Non-syndromic retinitis pigmentosa. *Prog Retin Eye Res*. 2018;66:157–186.

Investigative Ophthalmology & Visual Science